JCI insight

Restoring calcium homeostasis in Purkinje cells arrests neurodegeneration and neuroinflammation in the ARSACS mouse model

Andrea Del Bondio, … , Angelo Quattrini, Francesca Maltecca

JCI Insight. 2023. https://doi.org/10.1172/jci.insight.163576.

Research In-Press Preview Cell biology Neuroscience

Graphical abstract

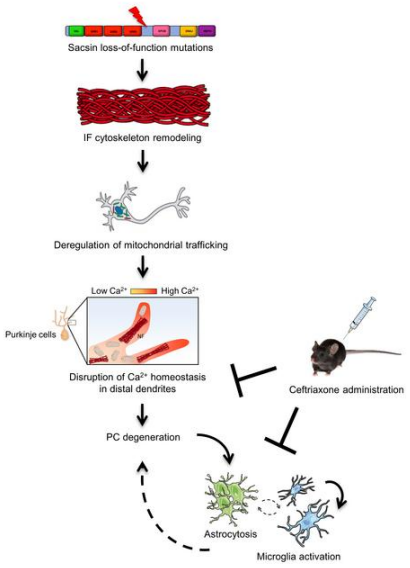

Restoring calcium homeostasis in Purkinje cells arrests neurodegeneration and neuroinflammation in the ARSACS mouse model

Andrea Del Bondio[1], Fabiana Longo[1], Daniele De Ritis[1,2], Erica Spirito[1,2], Paola Podini[3], Bernard Brais[4], Angela Bachi[5], Angelo Quattrini[3] and Francesca Maltecca[1,2]*

1. Mitochondrial Dysfunctions in Neurodegeneration Unit, Ospedale San Raffaele, Milan, Italy;

2. Università Vita-Salute San Raffaele, Milan, Italy.

3. Experimental Neuropathology Unit, Division of Neuroscience and Institute of Experimental Neurology, Ospedale San Raffaele, Milan, Italy;

4. Department of Neurology and Neurosurgery, Montreal Neurological Institute and Hospital, McGill University, Montreal, QC, Canada

5. IFOM- FIRC Institute of Molecular Oncology, Milan, Italy.

*Correspondence to: Francesca Maltecca, Mitochondrial Dysfunctions in Neurodegeneration Unit, Division of Neuroscience, Ospedale San Raffaele & Università Vita-Salute San Raffaele, Milan, Italy. Tel +39-02-2643.9116. email:maltecca.francesca@hsr.it.

The authors have declared that no conflict of interest exists

Abstract

Autosomal Recessive Spastic Ataxia of Charlevoix-Saguenay (ARSACS) is caused by mutations in *SACS* gene encoding sacsin, a huge protein highly expressed in cerebellar Purkinje cells (PCs). ARSACS patients, as well as mouse models, display early degeneration of PCs, but the underlying mechanisms remain unexplored, with no available treatments.

In this work, we demonstrated aberrant calcium (Ca^{2+}) homeostasis and its impact on PC degeneration in ARSACS. Mechanistically, we found pathological elevation in Ca^{2+}-evoked responses in *Sacs*$^{-/-}$ PCs, as the result of defective mitochondria and ER trafficking to distal dendrites and strong downregulation of key Ca^{2+} buffer-proteins. Alteration of cytoskeletal linkers, that we identified as specific sacsin interactors, likely account for faulty organellar trafficking in *Sacs*$^{-/-}$ cerebellum.

Based on this pathogenetic cascade, we treated *Sacs*$^{-/-}$ mice with Ceftriaxone, a repurposed drug which exerts neuroprotection by limiting neuronal glutamatergic stimulation, and thus Ca^{2+} fluxes into PCs. Ceftriaxone treatment significantly improved motor performances of *Sacs*$^{-/-}$ mice, at both pre- and post-symptomatic stages. We correlated this effect to restored Ca^{2+} homeostasis, which arrests PC degeneration and attenuates secondary neuroinflammation. These findings disclose new key steps in ARSACS pathogenesis and support further optimization of Ceftriaxone in pre-clinical and clinical settings for the treatment of ARSACS patients.

Keywords: autosomal recessive spastic ataxia of Charlevoix-Saguenay, pre-clinical trial, Purkinje cells, calcium, neuroinflammation

Introduction

ARSACS (MIM #270550) is a childhood-onset neurodegenerative disease characterized by cerebellar ataxia, followed by pyramidal tract signs and peripheral neuropathy (1, 2). ARSACS is caused by loss-of-function mutations in *SACS* gene, with more than 200 mutations identified worldwide (3).

The *SACS* gene encodes the massive 520 kDa protein sacsin, which is mainly expressed in the central nervous system, with the highest levels in PCs in the cerebellum (4-6). Loss of PCs is indeed the most prominent pathological feature in ARSACS patients (1) and in mouse models (*Sacs*$^{-/-}$ and *Sacs*$^{R272C/R272C}$). These models recapitulate the human phenotype presenting with ataxia in the early phases of disease, while spasticity and peripheral neuropathy occur at later stages (6-8).

Sacsin is a multimodular protein composed of an ubiquitin-like (UbL) domain that binds to the proteasome (5), three sacsin repeating regions (SRR) having high homology with Hsp90 (9), an XPCB domain (10), a DnaJ domain that binds Hsc70 (5), and a HEPN domain (11). Despite the nature of these motifs suggests that sacsin may operate in protein quality control, the cellular function of this protein and the pathophysiological consequences of its dysfunction remain largely unknown.

We previously found that the absence of sacsin impacts on intermediate filament (IF) organization, with abnormal bundles of vimentin in ARSACS-patient fibroblasts (12) and of neurofilament (NFs) in brain autopsies of ARSACS patients and in the *Sacs*$^{-/-}$ mouse (8).

Mitochondrial dysfunction was also reported in cell models of ARSACS, with reduced oxygen consumption rates (OCR), and increased reactive oxygen species (ROS) production (13, 14). A more interconnected mitochondrial network was observed in the same cell models and in dissociated dorsal root ganglia (DRG) neurons from the *Sacs*$^{-/-}$ mouse (7, 8, 13).

However, if and how these phenotypes are mechanistically inter-linked and cause PC

degeneration remains unsolved. Published studies were mostly performed in cell models (fibroblasts, HEK or SH-SY5Y cells) that do not recapitulate the complexity of PC morphology and physiology, or in sacsin-depleted cultured neurons that are not primarily affected in the disease (hippocampal neurons (7) or DRGs (15)). Indeed, cerebellar PCs are highly specialized neurons characterized by unique firing properties, high rate of metabolism and an extreme cyto-architecture, with an extensively branched dendritic tree receiving mostly glutamatergic stimulation (16).

Up to now, a detailed study of the mechanisms underlying PC degeneration is lacking, thus impeding the development of targeted treatments for ARSACS.

In this work, by employing multiple experimental approaches in vivo in the cerebellum and ex vivo in primary PCs from the *Sacs*$^{-/-}$ mouse model, we uncovered key aspects of cerebellar degeneration in ARSACS. We demonstrated for the first time a strong alteration of Ca^{2+} homeostasis in *Sacs*$^{-/-}$ mice. Our results suggest that this phenotype could be secondary to defective mitochondria and ER trafficking to distal dendrites, likely as the result of alterations in specific cytoskeletal linker proteins involved in organellar transport. Moreover, many proteins related to the regulation of Ca^{2+} homeostasis (Ca^{2+} buffers and Ca^{2+}ATP-ases) resulted strongly reduced in *Sacs*$^{-/-}$ mice. We also found that Ca^{2+}-induced PC degeneration triggers a neuroinflammatory response in cerebellum, with pronounced astrocytosis and microgliosis, supported by both immunohistochemistry and RNA sequencing data.

As a proof of concept of this pathogenetic cascade, we showed that the post- and pre-symptomatic administration of Ceftriaxone, a drug able to reduce glutamatergic stimulation and thus Ca^{2+} influx in neurons (17, 18), ameliorates motor symptoms and arrests PC degeneration in the *Sacs*$^{-/-}$ mouse. We demonstrated that this beneficial effect is likely achieved by restored Ca^{2+} homeostasis in PCs and attenuated neuroinflammation in cerebellum. Optimized Ceftriaxone treatment might represent a therapeutic perspective for ARSACS.

Results

Sacs$^{-/-}$ PCs show defective trafficking of mitochondria and ER

Sacs$^{-/-}$ mice display an early accumulation of non-phosphorylated NFH (npNFH) in the cerebellum at P15 (**Supplemental Figure 1A**). To dissect mechanistically the downstream effects of npNFH accumulation at a cellular level, we employed (i) *SACS*$^{-/-}$ SH-SY5Y cells that we previously generated (19) and (ii) *Sacs*$^{-/-}$ primary cerebellar cultures enriched in PCs. By confocal imaging, we demonstrated a striking IF accumulation in *SACS*$^{-/-}$ SH-SY5Y cells, both undifferentiated (vimentin and npNFH) (**Supplemental Figure 1B**) and differentiated into neurons (npNFH) (**Supplemental Figure 1C**). We also observed npNFH accumulation in *Sacs*$^{-/-}$ PCs in primary cerebellar cultures, that was evident in axon and proximal dendrites at DIV10 (**Supplemental Figure 2A**) and even more prominent at DIV15, a stage at which PCs are arborized and spiny (**Supplemental Figure 2B**). At this stage, the morphology of *Sacs*$^{-/-}$ and wild-type PCs was comparable, as supported by unchanged total volume (**Supplemental Figure 2C**). No major defects in microtubules and microfilaments were observed in *SACS*$^{-/-}$ SH-SY5Y cells differentiated into neurons as well as in *Sacs*$^{-/-}$ primary PCs (**Supplemental Figure 2, D-F**), indicating IF remodeling as a primary event in ARSACS pathogenesis.

Since *Sacs*$^{-/-}$ primary PCs nicely recapitulate the in vivo ARSACS pathophysiology, we next explored if npNFH accumulation in proximal dendrites may impact organelle trafficking to the periphery.

We first focused on mitochondria, which are essential for ATP supply and Ca^{2+} buffering in distal dendrites of PCs, receiving massive glutamatergic stimulation (18, 20). Long-range transport of mitochondria occurs along microtubules, while actin filaments and NFs mediate short-range movement, docking and transient immobilization (21).

By immunofluorescence staining and 3D reconstruction of confocal stack images, we found that mitochondria were retained in the cell soma and not properly distributed in distal dendrites

of *Sacs*$^{-/-}$ PCs at DIV15. Indeed, quantitative image analysis showed that the volume of mitochondria in PC dendrites was significantly reduced in *Sacs*$^{-/-}$ neurons compared to wild-type controls, while the volume of mitochondria in the soma was increased (**Figure 1A**). To complement this volumetric analysis, we performed live imaging of mitochondrial movement in PCs by infecting primary cerebellar cultures with mtDsred2. PCs were clearly distinguished in brightfield for their peculiar morphology, as they were markedly larger and more ramified than granule cells or inhibitory interneurons. Quantitative analysis showed that both retrograde and anterograde movement rate were significantly reduced in *Sacs*$^{-/-}$ versus *Sacs*$^{+/+}$ PCs, as well as the total distance travelled by each mitochondrion (**Figure 1B and Supplemental Figure 3A**). No differences were found in total PC mitochondrial volume (normalized to total PC volume) (**Supplemental Figure 3B**). In agreement, mitochondrial biogenesis resulted unaffected in *Sacs*$^{-/-}$ mice compared to *Sacs*$^{+/+}$ mice, as demonstrated by unaltered levels of the master regulator of this pathway (PGC1-α (22), both mRNA and protein) and of its downstream targets *Nrf1* and *Nrf2* (**Supplemental Figure 3, C and D)**.

We demonstrated that cytoskeletal disorganization in the absence of sacsin also impacts ER, which is crucial in PC spines as well as mitochondria in local Ca^{2+} storage and synaptic plasticity (23, 24). Immunofluorescence assay followed by volumetric analysis revealed reduced amount of ER into dendrites of *Sacs*$^{-/-}$ PCs versus wild-type controls at DIV15. As for mitochondria, the volume of ER in the soma was increased, while no differences were found in total PC ER volume (normalized to total PC volume) (**Figure 1C** and **Supplemental Figure 3E**). The thinness of the PC axon prevented us from performing organellar volumetric analysis, as done in dendrites.

To further confirm a failure in organelle transport in vivo in the absence of sacsin, we purified synaptosomal fractions from cerebellum and quantified structural markers of mitochondria (AFG3L2) and ER (calreticulin) by WB. This analysis unraveled a slight but significant

reduction of these proteins in synaptosomes derived from *Sacs*$^{-/-}$ cerebellum compared to wild-type controls (**Supplemental Figure 3F**).

Mitochondrial ultrastructure and functionality are not altered in *Sacs*$^{-/-}$ cerebellum

Previous papers showed altered mitochondrial respiration in ARSACS patient fibroblasts and in *SACS* knockdown SH-SY5Y cells (13, 14). We thus tested if this defect is conserved in cerebellum in the absence of sacsin. We performed electron microscopy (EM) analysis of PC soma and synaptic terminals in vivo to visualize mitochondrial ultrastructure. High resolution images underlined intact inner and outer membranes, with well-defined cristae organisation both in wild-type and in *Sacs*$^{-/-}$ PCs at 5 months of age (**Figure 2A**). Quantitative analysis of several mitochondrial structure parameters revealed no differences between *Sacs*$^{-/-}$ and *Sacs*$^{+/+}$ cerebellum (**Figure 2A** and **Supplemental Figure 3G)**. We also tested mitochondrial ATP production in freshly isolated mitochondria from cerebellum of *Sacs*$^{-/-}$ mice and relative wild-type controls at the same age. We found no differences in mitochondrial ATP levels produced by *Sacs*$^{-/-}$ mice compared to wild-type, both at basal state and upon stimulation with pyruvate (**Figure 2B**). To exclude that this result could reflect a dilution effect of PCs in total cerebellum, we assayed respiratory chain functionality by COX (**Figure 2C**) and SDH (**Figure 2D**) enzymatic assays in situ on cerebellar cryostat sections, which however revealed no differences in *Sacs*$^{-/-}$ PCs compared to wild-type samples.

To further strengthen these results, we evaluated mitochondrial ultrastructure and functionality in *Sacs*$^{-/-}$ primary PCs. Ultrastructural EM analysis revealed intact morphology and cristae, in both soma and dendrites, in agreement with in vivo data (**Figure 2E** and quantitative analysis is reported in **Supplemental Figure 3H**). We then tested $\Delta\Psi_{mito}$ by live-imaging measurement of the potentiometric dye Tetramethylrhodamine (TMRM), which revealed no changes in *Sacs*$^{-/-}$ PCs versus wild-type controls at DIV15 (**Figure 2F**).

Altogether, these results suggest that, although inefficiently trafficked, mitochondria are metabolically unaltered in *Sacs*$^{-/-}$ primary PCs as well as in vivo at 5 months, a stage in which motor defects are already manifested in the ARSACS mouse model.

Alteration of cytoskeletal linkers mediating organellar transport in the absence of sacsin

To try to find a mechanistic link between sacsin, NF accumulation and impaired organellar trafficking, we immunoprecipitated endogenous sacsin to identify its interactors. Since both cerebellum and primary cerebellar cultures are heterogeneous in terms of cell populations, with several non-neuronal components, we employed SH-SY5Y cells differentiated into neurons, which express considerable levels of sacsin and that recapitulate npNFH accumulation.

Immunoprecipitation (IP) of sacsin in wild-type SH-SY5Y cells differentiated into neurons, followed by Label Free Quantitative (LFQ)-Mass Spectrometry (MS) of eluates, identified 67 specific sacsin interactors (absent in *SACS*$^{-/-}$ SH-SY5Y cells used as negative controls, where IP was performed using the same anti-sacsin Ab) (**Figure 3A and Supplemental Table 1**). STRING network and enrichment analysis underlined that sacsin physical interactors cluster in specific categories related to supramolecular fiber, actin filament & cytoskeleton organization and organelle localization (**Supplemental Figure 4A**), supporting the hypothesis that sacsin may exert quality control on cytoskeletal proteins that are crucial for trafficking in highly polarized cells like neurons. NFL and NFM subunits were found directly interacting with sacsin (**Table in Figure 3**), whereas no resident mitochondrial proteins were identified, suggesting that sacsin does not directly interact with mitochondria. Interestingly, among sacsin interactors we found plectin, a 534 kDa multifunctional cytolinker protein that connects IF with other cytoskeletal components and mitochondria (25, 26), and myosin Va, a 215 kDa protein crucial for both mitochondrial and ER transport in PC dendrites (24) (**Table in Figure 3**). Based on our imaging studies revealing NF bundles and defective organellar trafficking in PCs

without gross defects in microtubules and microfilaments, we decided to focus on these interactors. We re-confirmed the interaction between NFL and sacsin, myosin Va and sacsin in SH-SY5Y cells (**Figure 3, B and C**), and between sacsin and plectin in both SH-SY5Y cells and in cerebellum (**Figure 3, D and E**). In support to a potential plectin involvement in ARSACS pathogenesis, we found reduced plectin levels in soluble fractions obtained from a panel of ARSACS patient fibroblasts harboring different *SACS* mutations (**Supplemental Figure 4B**), in two different clones of *SACS*$^{-/-}$ SH-SY5Y cells (**Supplemental Figure 4C**), and in *Sacs*$^{-/-}$ cerebellum (**Supplemental Figure 4D**). According to our data, plectin is not reduced per se, rather it is redistributed in the insoluble-cytoskeletal fraction. Indeed, the WB on total homogenates from ARSACS patients' cells, by lysis of whole cellular pellets in Laemmli buffer 2X and loading on mixed acrylamide-agarose gels (that allows to detect putative aggregates up to 600 kDa complexes (27)) show that plectin itself increased drastically in total homogenates patients' cells compared to controls, as well as vimentin (**Supplemental Figure 4E**). Similarly, the absence of sacsin impacts on plectin and myosin Va (which is neuronally expressed) solubility in vivo, as both proteins increase in the Triton-x100 insoluble fractions from *Sacs*$^{-/-}$ cerebellum, compared to wild-type littermates (**Figure 3F**). To support these biochemical data, we performed plectin immunofluorescence on murine cerebellar sections at 5 months of age. Plectin showed a more intense signal in the soma and proximal dendrites of *Sacs*$^{-/-}$ PCs compared to wild-type samples, in overlap with the NF bundles (**Figure 3G and Supplemental Figure 5A**). Interestingly, npNFH or plectin immunofluorescence combined with sacsin staining in primary PCs revealed an overlap of the two signals (**Supplemental Figure 5, B and C**). Altogether, these results indicate that in the absence of sacsin, there is a striking remodeling of cytoskeletal proteins involved in organellar movement, that could lead to a failure in global intracellular trafficking.

Sacs$^{-/-}$ primary PCs show defective cytosolic Ca^{2+} handling

A fine regulation of free cytosolic Ca^{2+} concentration is crucial in PCs, which receive massive Ca^{2+} influxes in post-synaptic dendrites due to glutamatergic stimulation.

Post-synaptically, Ca^{2+} signals are shaped by cooperation of Ca^{2+}-binding proteins, ER and mitochondria (28). Mitochondria accumulate Ca^{2+} into the matrix themselves, but also fuel Ca^{2+} clearance systems, i.e. Ca^{2+} ATP-ases in the plasma membrane and ER (29).

Given the reduced presence of mitochondria and ER in terminal dendrites of *Sacs*$^{-/-}$ PCs, we performed live Ca^{2+} imaging by using the highly sensitive Ca^{2+} probe Calbryte^{TM} 520 in primary cerebellar cultures at DIV15. Upon challenge with 30 mM KCl, which promotes Ca^{2+} entry by plasma membrane and empties Ca^{2+} stores, we found that the Ca^{2+}-evoked peaks ($\Delta F/F_0$) were significantly increased in *Sacs*$^{-/-}$ PCs compared to wild-type (**Figure 4A**), reflecting a defective capacity of *Sacs*$^{-/-}$ PCs to handle Ca^{2+} influxes. This was specific to PC, as Ca^{2+}-evoked responses in *Sacs*$^{-/-}$ granule cells in the same cerebellar cultures were comparable to wild-type (**Figure 4B**).

Integrated -OMICS approaches disclose deregulation of Ca^{2+} homeostasis in *Sacs*$^{-/-}$ cerebellum

To further explore the potential involvement of Ca^{2+} deregulation in ARSACS pathogenesis, we applied two -OMICS approaches in vivo. Firstly, performing LFQ proteomics on cerebellum at 5 months of age (post-symptomatic stage), we identified 194 proteins that were differentially expressed in *Sacs*$^{-/-}$ mice versus controls (44 upregulated and 150 downregulated) (**Figure 4C and Supplemental Table 2**). Gene Ontology (GO) enrichment analyses revealed the deregulation of many proteins related to ion transmembrane transport and in particular to Ca^{2+}-transport, synaptic transmission and signalling (**Figure 4D**). Most proteins belonging to microfilaments and microtubules were unaltered, while we found a strong downregulation of

proteins related to Ca^{2+} homeostasis, such as Inositol 1,4,5-trisphosphate receptor type 1 (IP3R1, also validated by WB-**Figure 4E**), Ca^{2+} ATP-ases (ATP2B2, ATP2A3, ATP2A2) and Ca^{2+}-binding proteins (calbindin, also validated by WB-**Figure 4F)**. This reduction is specific and not due to PC loss, as a specific marker of PCs (PCP2, also validated by WB-**Figure 4F**) remained unaltered **(Supplemental Table 2**). The increase of Ca^{2+} concentration is known to promote Ca^{2+}-calmodulin-dependent protein kinase type II subunit beta (CaMKIIβ) autophosphorylation (30). We thus tested the phosphorylation state of CaMKIIβ, which was drastically increased in *Sacs*$^{-/-}$ samples in comparison to wild-type controls despite unchanged amount of CaMKIIβ (**Figure 4G**), further enforcing a deregulation of Ca^{2+} in *Sacs*$^{-/-}$ cerebellum.

We then performed RNA sequencing (RNA seq) analysis on *Sacs*$^{-/-}$ cerebellar bulk RNA extracts compared to age-matched wild-type controls at 5 months of age. This analysis revealed 137 deregulated genes in *Sacs*$^{-/-}$ cerebellum (59 upregulated and 78 downregulated) (**Figure 5A and Supplemental Table 3**). GO analysis highlighted that most downregulated genes in the absence of sacsin belong to ion channel transport and activity (GO: MF) and cation transport (GO: BP), further highlighting a specific Ca^{2+} deregulation (**Figure 5B**). Interestingly, *Itpr1* and *Calb1* transcripts were downregulated, in agreement with their reduced protein levels. In addition, we found reduction of other transcripts encoding Ca^{2+} related proteins, such as *Casq2, Car8 and Trpc3* (**Figure 5C and Supplemental Table 3**).

PC degeneration in *Sacs*$^{-/-}$ cerebellum is associated to neuroinflammation

GO analysis of RNA seq data revealed that the most upregulated genes in *Sacs*$^{-/-}$ cerebellum were involved in inflammatory response and cytokine production (GO: BP) (**Figure 5, A and B**), indicating a neuroinflammatory process accompanying PC death.

Consistent with the activation of reactive astrogliosis, GFAP resulted increased at both protein level (measured by WB and LFQ proteomics) and mRNA level (measured by qPCR and RNA seq) at 5 months of age (**Figure 5, D and E, and Supplemental Table 2 and 3**). Immunofluorescence staining documented an increased GFAP signal in *Sacs*$^{-/-}$ cerebellum compared to wild- type, especially in the most internal part of cerebellum where the majority of glial cells resides (**Figure 5F**) (31). These results unlikely reflect a direct role of sacsin on astrocytic IF (GFAP), as indicated by unchanged GFAP levels at 1 month in *Sacs*$^{-/-}$ cerebellum (**Supplemental Figure 6, A and B**) and by unaltered GFAP staining in astrocytes in *Sacs*$^{-/-}$ primary cerebellar cultures versus wild-type (**Supplemental Figure 6C**).

In addition, many genes typical of the phagocytic microglia (*Itgax*, *Clec7a*, *Cd68*, *Trem2*, *Lpl Pycard*, *Tyrobp*) resulted strongly upregulated by RNA seq analysis (**Supplemental Table 3)**. These findings were complemented by immunostaining for the microglial marker Iba1, which revealed a drastic proliferation of microglia and a morphological shift of the microglia towards an amoeboid-phagocytic phenotype in *Sacs*$^{-/-}$ slices compared to the homeostatic phenotype of the wild-type (**Figure 5G)**.

Interestingly, the most upregulated gene in *Sacs*$^{-/-}$ cerebellum was *Lcn2* (**Supplemental Table 3**) encoding for Lipocalin-2, a multifunctional protein synthesized and secreted as an inducible factor from activated microglia, reactive astrocytes, neurons, and endothelial cells in response to brain insults. Several components of the complement system *(C3*, *C3ar1*, *C4b*, *C1qa*, *C1qb* and *C1qc*), part of brain-innate immune system, were also found strikingly upregulated (**Supplemental table 3**).

Altogether, these data support the activation of a neuroinflammatory response which accompanies PC degeneration in *Sacs*$^{-/-}$ cerebellum.

Ceftriaxone administration in *Sacs*$^{-/-}$ mice ameliorates motor ability and delays PC loss by improving Ca^{2+} homeostasis and neuroinflammation

Ceftriaxone is a β-lactam antibiotic able to efficiently pass the blood-brain barrier, which is used clinically to treat certain paediatric meningitis. There is robust evidence that Ceftriaxone exerts neuroprotection in many pre-clinical models of neurodegeneration acting by multiple mechanisms (32, 33). Several studies have documented Ceftriaxone ability to reduce glutamate concentration at inter-synaptic space and consequently Ca^{2+} levels post-synaptically (17), including PCs (18, 34). This evidence provided us a strong rationale to test Ceftriaxone in the ARSACS pre-clinical model, given the deregulation of Ca^{2+} homeostasis that we documented. As most diagnosed ARSACS patients are already symptomatic at the time of diagnosis, we first designed a post-symptomatic trial in *Sacs*$^{-/-}$ mice. We administered the drug starting at 5 months of age, a stage at which PC loss and motor symptoms are already evident (8). Mice were treated by intraperitoneal (i.p.) injection with 200 mg/kg of Ceftriaxone for 5 consecutive days. In this trial only two cycles of administration (5 and 6 months) were performed (**Figure 6A**). Before drug administration, we assessed motor incoordination and balance deficit of *Sacs*$^{-/-}$ mice by beam walking (BW) test, which confirmed reduced performances of *Sacs*$^{-/-}$ females and males in terms of latency to cross the beam and hindfoot missteps compared to age- and sex-matched wild-type controls, as previously described (8) (**Supplemental Figure 7A**). At 7 months, we observed a clear progression of the disease in *Sacs*$^{-/-}$ mice treated with vehicle (when compared with their performances at 5 months old mice), which was instead curbed in *Sacs*$^{-/-}$ mice treated with Ceftriaxone. The latency time to cross the beam and the number of hindlimb missteps were remarkably reduced both in *Sacs*$^{-/-}$-treated females (**Figure 6B**) and males (**Supplemental Figure 7B**) compared to vehicle treated mice. Semithin sections of anterior lobules of *Sacs*$^{-/-}$ Ceftriaxone-treated mice underlined an attenuation of PC degeneration when compared with vehicle-treated *Sacs*$^{-/-}$ controls (**Figure 6C**). By WB

analyses of cerebellar extracts, we found that Ceftriaxone treatment strikingly reduces the pathological hyperphosphorylation of CaMKIIβ in *Sacs*$^{-/-}$ mice (**Figure 6D**). We also observed that the levels of the Ca^{2+} buffers calbindin and parvalbumin, and of IP3R1 are increased by Ceftriaxone treatment (**Supplemental Figure 7, C and D**). These results support that Ceftriaxone ameliorates the motor phenotype and delays PC degeneration in *Sacs*$^{-/-}$ mice by acting on cytosolic Ca^{2+} homeostasis, while it is not effective on the accumulation of npNFH (**Figure 6D**). Moreover, we showed evidence supporting that Ceftriaxone administration attenuates astrogliosis, as showed by decreased *Gfap* mRNA (**Figure 6E**) as well as GFAP-positive signal in the white matter of the cerebellum (**Figure 6F**) in Ceftriaxone-treated *Sacs*$^{-/-}$ cerebellum compared to vehicle-treated controls.

We also tested Ceftriaxone efficacy at pre-symptomatic stages, before the onset of disease symptoms. In this pre-clinical trial, the administration protocol consisted in the same regimen as in the post-symptomatic trial, but the drug was administered starting at 1 month until 5 months of age (5 cycles of administration) (**Figure 7A**). At 6 months of age, motor assessment by BW test showed an evident improvement of *Sacs*$^{-/-}$ Ceftriaxone-treated mice both in latency time to cross the beam and in number of hindlimb missteps compared to placebo-treated age- and sex-matched controls (**Figure 7B, and Supplemental Figure 8A**). Moreover, semithin section analysis demonstrate a reduced PC loss in *Sacs*$^{-/-}$ Ceftriaxone-treated cerebellar (anterior lobules) versus vehicle-treated animals (**Figure 7C**). During both trials, we monitored body weight of treated and untreated mice and we found no significant differences between the two groups (**Supplemental Figure 8, B and C**). In the pre-symptomatic trial, the results of haematocrit did not disclose any altered parameter in treated mice. No clear toxicity was observed based on normal values for blood urea, creatinine, albumin and transaminases ALT parameters, together supporting that repeated Ceftriaxone treatment did not impact kidney or

liver function (**Supplemental Table 4**). In conclusion, Ceftriaxone administration in the ARSACS mouse model with the adopted 5 days a month-posology appears effective and safe.

Discussion

In this work, we shed light on the molecular mechanisms underlying PC death in ARSACS and provided evidence of the efficacy of Ceftriaxone in the *Sacs*$^{-/-}$ mouse model. The combination of complementary experimental strategies and different models (in vitro, ex vivo and in vivo), integrated with -OMICS approaches allowed us to better dissect the cascade of events downstream to the absence of sacsin that leads to PC degeneration.

Although it is well established that loss of sacsin causes IF cytoskeleton derangement in different cell types (6, 12, 15), how this phenotype causes PC degeneration was still unclear. The accumulation of npNFH has been observed in different neurons, but only PCs were found to degenerate in the *Sacs*$^{-/-}$ mouse model (8), highlighting a selective susceptibility of these cells in ARSACS. Our data showed an early and striking npNFH accumulation in proximal dendrites and axons of *Sacs*$^{-/-}$ primary PCs, making these cultures ideal to dissect the downstream consequences of cytoskeletal remodeling. In these neurons, we showed evidence supporting defective mitochondria and ER trafficking to distal dendrites and Ca^{2+} deregulation in these sites, which is likely to cause PC degeneration in ARSACS.

Previous studies in cell models showed alteration of oxidative phosphorylation and mitochondrial morphology in the absence of sacsin. (7, 13, 14) Our ex vivo and in vivo data in *Sacs*$^{-/-}$ PCs indicate that mitochondrial morphology is comparable between *Sacs*$^{-/-}$ mice and controls, with no signs of hyperfusion or ultrastructural alterations. Accordingly, mitochondrial ATP production was unaltered in *Sacs*$^{-/-}$ total cerebellum, as well as COX and SDH activity measured specifically in PCs at 5 months of age, when neurodegeneration is overt.

Although mitochondrial transport occurs mostly on microtubules and actin filaments, there is growing evidence that IF contribute to mitochondrial localization in different cell types, including neurons (35). Transgenic mouse models in which NFs are perturbed show aberrant mitochondrial motility (36, 37). Moreover, extensive dephosphorylation of NFH subunits affects their interaction with mitochondria leading to a reduced rate of mitochondrial motility (38). These pieces of evidence further support our hypothesis that npNFH accumulation in proximal dendrites of *Sacs*$^{-/-}$ PCs could conceivably restrict mitochondrial movement. By live imaging analysis of mitochondrial movement in primary PCs, we indeed found a reduction in both the anterograde and retrograde transport of mitochondria in *Sacs*$^{-/-}$ mice versus controls. This is in agreement with a recent paper reporting altered lysosomal positioning in ARSACS fibroblasts and *Sacs*$^{-/-}$ mouse cortical neurons (39), that the authors correlate to alteration in microtubule dynamics. Although we could not appreciate gross defects in microtubules in *SACS*$^{-/-}$ SH-SY5Y cells as well as ex vivo in *Sacs*$^{-/-}$ PCs, and LFQ proteomics in *Sacs*$^{-/-}$ cerebellum did not reveal any change in microtubule-related proteins, we cannot exclude that other molecular alterations in microtubules can occur as a consequence of NF bundling.

While the displacement of mitochondria and other organelles to the periphery of vimentin bundles in ARSACS fibroblasts (12) is consistent with our hypothesis of a primary and direct role of sacsin in regulating IF cytoskeleton, the altered mitochondrial functionality observed in ARSACS cell models (7, 13, 14) may rather reflect a secondary effect highlighted by culture conditions, that could be milder or more difficult to appreciate in vivo in the *Sacs*$^{-/-}$ mouse. Also, most of the specific sacsin interactors that we identified by IP experiments were large cytoskeletal proteins, including NFL and NFM, while no mitochondrial proteins were detected. In addition to NFs, plectin and myosin Va were found to directly interact with sacsin. Plectin is a giant multifunctional protein acting as a mechanical linker between IF network and other cytoskeletal structures, as well as mitochondria (25). Plectin deficiency was demonstrated to

impact on mitochondrial shape and mostly on its transport (26, 40). Class V myosins are actin-based motors that mediate the proper short-range intracellular transport of diverse organelles, mRNAs and proteins (41). Myosin Va is expressed at high levels in PCs (23) and its deficiency in PCs showed drastic organelle localization defects, as demonstrated by ER missing specifically from dendritic spines (24). Our data showing alterations in mitochondria and ER distribution in distal dendrites in *Sacs*$^{-/-}$ primary PCs phenocopy plectin or myosin Va deficiency in neurons, supporting the potential involvement of these two proteins in ARSACS pathogenesis (24, 26). We also uncovered accumulation of plectin in cerebellar insoluble fractions from *Sacs*$^{-/-}$ mouse cerebellum and, consistently, increased plectin signal in somato-dendritic regions of *Sacs*$^{-/-}$ PCs, overlapping the NF bundles. If this could reflect a direct role of sacsin on protein quality control of plectin, as well as NFs, needs to be clarified. Further biochemical and functional studies are required to elucidate this point, which is anyway difficult to be addressed endogenously in vivo considering the enormous sizes and stickiness of these cytoskeletal proteins and the possible transient nature of these interactions.

We provided several lines of evidence that Ca^{2+} homeostasis is altered in *Sacs*$^{-/-}$ PCs. The control of Ca^{2+} homeostasis is crucial in PCs, since it regulates autonomous pacemaking, as well as spiking induced by synaptic input (42). Many cerebellar ataxias indeed show alteration of Ca^{2+} homeostasis as pathogenetic converging mechanism (43, 44). Ca^{2+} imaging experiments disclosed higher cytosolic Ca^{2+}-peak responses upon KCl stimulation in *Sacs*$^{-/-}$ PCs compared to wild-type. Deregulated Ca^{2+} homeostasis at synapses in the absence of sacsin likely results from ineffective Ca^{2+} buffering due to deprivation of mitochondria and ER, but also from reduced levels of ATP in these sites, that can impact Ca^{2+} ATP-ase functionality. In vivo, we detected a specific increase of phosphorylation state of CaMKIIβ in *Sacs*$^{-/-}$ cerebellum, and downregulation of many Ca^{2+} related proteins, including Ca^{2+} ATP-ases, Ca^{2+} binding proteins and IP3R1.

We also found a striking upregulation of mRNAs typical of the phagocytic microglia and of reactive astrocytes, indicating a neuroinflammatory process accompanying PC degeneration. These findings were complemented by immunofluorescence analyses, showing typical changes in morphology of these glial cells during the neurodegeneration (45, 46). There is growing evidence that microglia may contribute to cerebellar vulnerability in ataxias (47), however further studies are needed to dissect the role of neuroinflammation as potential modifier of disease progression in ARSACS.

Deregulated Ca^{2+} homeostasis in *Sacs*$^{-/-}$ PCs and cerebellum provided us the rationale to test Ceftriaxone efficacy in the ARSACS mouse model. It is indeed well documented that this drug limits glutamatergic stimulation of neurons, reducing Ca^{2+} influx post-synaptically (32), although some papers propose its neuroprotective action through increased antioxidant response and attenuated neuroinflammation (32). We decided to administer Ceftriaxone intraperitoneally at a regimen already effectively proven to target cerebellum (18, 34). Drug treatment resulted successful in symptomatic *Sacs*$^{-/-}$ mice, as it delayed PC loss and attenuated reactive astrogliosis, with a clear arrest of motor impairment progression. The beneficial effect of Ceftriaxone was likely due to its action on Ca^{2+} levels, as shown by normalized phosphorylation state of CaMKIIβ and by the restoration of IP3R1, calbindin and parvalbumin levels in the cerebellum of treated *Sacs*$^{-/-}$ mice. Ceftriaxone was previously shown to act modulating the transcription of GLT1 through NF-kB (48). Our in silico analysis highlighted NF-kB putative binding sites in the promoter region of *Itpr1*, *Calb1* and *Pvalb*, suggesting that a similar mechanism could account of the increased levels of these proteins upon Ceftriaxone treatment (**Supplemental figure 7E**).

Encouraging results were obtained also with the pre-symptomatic Ceftriaxone treatment (starting at 1 month of age), where we tested the possibility to prevent or delay ARSACS disease progression. The outcomes obtained seem not to be significantly different compared

with post-symptomatic treatment, suggesting that they both delay PC loss and motor defect. Two possible explanations could be that Ceftriaxone did not target the earliest upstream events of ARSACS pathogenesis (i.e., npNFH accumulation and/or others that are still undefined), and/or that maybe administration at 1 month of age is already too late to start the treatment, as the molecular pathomechanisms are already activated. In fact, although few papers showed that Ceftriaxone is able to resolve protein aggregates (49, 50), it did not rescue the npNFH accumulation in *Sacs*$^{-/-}$ mice.

ARSACS is the second most common form of recessive ataxia worldwide and no disease-modifying treatment is available for this disabling disorder. Our data on Ceftriaxone efficacy in the ARSACS mouse model offers the first therapeutic perspective for ARSACS patients in a close-to-human model. Although a clinical trial with Ceftriaxone failed in a cohort of ALS because of the toxic adverse reaction (it was administered via a central venous catheter, chronically at the dose of 4 g/day up to 30 months, and most patients assumed Riluzole at the same time (51)), our data show that the chronic use of Ceftriaxone may be not necessary in a clinical trial in ARSACS. Therefore, a marked reduction of the dosage combined with a pulsed treatment could drastically reduce toxicity. Ceftriaxone may be also administered intramuscularly or subcutaneously, as employed in a clinical trial for Parkinson's disease, where they are administering Ceftriaxone by intramuscular injection at 1 g per day for Day 1, 3, and 5 per cycle on a 2-weekly cycle (https://clinicaltrials.gov/ct2/show/NCT03413384?term=ceftriaxone&draw=2&rank=3).

The efficacy of Ceftriaxone at post-symptomatic stages in the *Sacs*$^{-/-}$ mouse model encourages a future translation in clinics, as most ARSACS patients are diagnosed only after the onset of gait abnormalities. Many additional studies are of course needed to further advance Ceftriaxone treatments for ARSACS towards clinical application, especially in terms of dosage, route of

administration, duration of treatment, toxicity, and identification of non-invasive biomarkers that could help monitoring drug efficacy.

Methods

Immunofluorescence in primary PC cultures and cerebellar slices

Primary cerebellar cultures were derived as previously described. These are mixed cerebellar cultures containing PCs, astrocytes and other neurons, as required for PC survival and maturation (18). For immunofluorescence, fixed cells were incubated with the following primary antibodies: calbindin 28 kDa (CB300; Swant Inc.), calbindin (214011; Synaptic System GmbH), OxPhos complex IV subunit I (459600; Invitrogen), calreticulin (C4606; Sigma-Aldrich, Merck KGaA) and npNFH (SMI32, 801701; Calbiochem, Merck KGaA). Secondary antibodies conjugated with Alexa Fluor 488 and Alexa Fluor 546 (Invitrogen) were used.

Mice at 5 months of age were sacrificed in the presence of anaesthesia (2,2,2-Tribromoethanol, Sigma-Aldrich, Merck KGaA). Transcardially perfusion was performed and then the brain was isolated. Tissues were fixed in 4% paraformaldehyde (2h, 4°C), then dehydrated in 30% sucrose solution (over/night, 4°C) and finally included in OCT solution (Bio-Optica Milano). Cryostat sagittal slices were cut at the thickness of 20µm and conserved at -80°C. Immunofluorescence was performed as described for fixed primary PCs. For plectin and NFH, images were taken at FluoVIEW FV3000RS Confocal (Olympus) at 63X magnification and analyzed with Fiji-ImageJ software (https://imagej.net/Fiji). Antibodies used for immunostaining: plectin (sc-33649; Santa Cruz Biotechnology Inc.) and total NFH (ab1989; Millipore). For GFAP (Z0334; Dako, Agilent) and Iba1 (019-19741; Wako, Fujifilm), samples were imaged using DeltaVision Ultra (GE Healthcare, Chicago, USA) equipped with a 40X/NA0.8 objective lens (Olympus, Tokyo, Japan). For multi-colour imaging, z-stacks of

individual channels were sequentially acquired, after optimization of imaging parameters such as illumination parameters and exposure time. For larger fields of view, the samples were scanned at lateral steps of 349 um, i.e. with 10% overlap, and the collected images were computationally stitched as tile mosaic images using the grid/collection stitching plugin provided by the software package SoftWoRx provided by the microscope's manufacturer. During the process of figure assembling to create panels, original images (at the resolution of 0,167μm/pixel) were processed with Fiji software and resized by scaling the pixels by interpolation.

Volumetric analysis of primary PCs

Stacks of consecutive confocal images of immunofluorescence performed on primary PCs were taken at 0,1 μm intervals using the UltraVIEW Confocal Microscope (PerkinElmer). Analyses of soma, dendrite, mitochondria and ER volume were performed using Volocity 3D Image Analysis Software (version 5.5.1, PerkinElmer). For mitochondrial and ER volume evaluation, a region of interest (ROI) was drawn to cover the profile of each PC (or dendrites only). A threshold for red signal (mitochondria and ER) and green signal (PCs) was set to exclude the background. We considered mitochondria/ER belonging to PCs those with red signal exclusively intersecting the green signal.

Mitochondrial live imaging in primary cerebellar cultures

Primary PC cultures were obtained as described above. At DIV0, prior to plating, cells were infected with a lentivirus expressing mtDsRed2 (Clontech) at 1:200 concentration from 4.67*10^8 U/mL. Cells were plated on bottom-glass culture dishes (MatTek Corporation). At DIV10, real-time movies of mitochondria in PC-dendrites were acquired on a DeltaVision Ultra (GE Healthcare, Chicago, USA) microscope enclosed with a temperature and CO_2 incubation chamber. Images were acquired with a 60X/NA1.4 objective lens (Evident, Tokyo, Japan), every minute for 30 minutes. Images were first deconvolved with Huygens Professional version 19.04 (Scientific Volume Imaging, The Netherlands, http://svi.nl) and mitochondria tracking was performed with Arivis Vision4D (Version: 3.1.3, arivis AG Rostock, Germany). Before analysis, images were cropped and rotated to orientate the dendrite horizontally and keep the soma always on the left side of the image. A manual track tool was used to create a track interactively in the viewer. Output measurements were then exported in excel files for each track and analyzed for statistical significance. Kymographs were obtained with KimographClear plugin for Fiji (52), from time series of max-projections, according to user manual, where forward and backward motion correspond to anterograde and retrograde mitochondrial movement respectively.

EM analyses

EM analyses were done in collaboration with the Unit of Neuropathology of San Raffaele Institute as previously described (18) (Details in Supplemental Methods).

In vivo mitochondrial ATP assay

To measure mitochondrial ATP production in cerebellum, we isolated fresh mitochondria and applied the same experimental procedure as described in (53) (Details in Supplemental Methods).

Measurement of $\Delta\Psi_{mito}$

$\Delta\Psi_{mito}$ was measured using TMRM (Invitrogen) as previously described (18) (Details in Supplemental Methods). Images were analysed using Fiji software.

COX-SDH enzymatic assay

In situ activity staining were performed on cryostat sagittal slices according to manufacturer's instructions (Bio-Optica Milano). Images were acquired using Axio Imager.M2 (Zeiss) and analysed using Fiji software.

Immunoprecipitation

SH-SY5Y cells or cerebellum were collected and freshly lysed in lysis buffer (5 mM EDTA pH 8.0, Triton X-100 0,1% in PBS1X and PIC (Sigma-Aldrich, Merck KGaA) with a Dounce homogenizer. Total homogenate was centrifuged at 8000 g for 10' at 4°C. After a preclearing step, the IP antibody was bound to magnetic DynabeadsA or G (ThermoFisher Scientific) and the Dynabeads-antibody complex was incubated with the precleared lysate over/night at 4°C on a wheel. After washes in lysis buffer, the antigen was eluted in Urea 8 M Tris-HCl pH 8 on rotation for 30' for LC-MS/MS and/or WB or in Laemmli buffer following 10' rotation, and incubation at 100°C for 5', for WB.

For sacsin IPs, anti-sacsin antibody (181190; Abcam) was used; for plectin IP, anti-plectin (ab32528; Abcam) antibody was used; for NFL IP, anti-NFL antibody (8A1, sc-20012; Santa Cruz Biotechnology Inc.) was used. Anti-myosin (LF-18 M4812; Sigma-Aldrich, Merck KGaA), anti-plectin (ab32528; Abcam) and anti-NFL (8A1, sc-33649; Santa Cruz Biotechnology Inc.) antibodies were used for immunoblot. Mouse IgG1 (R&D Systems) or rabbit IgG (Sigma-Aldrich, Merck KGaA) were used as isotype controls.

Immunoprecipitated eluates were sent to LC-MS/MS and/or loaded on SDS-PAGE for WB analysis. Enrichment and network analyses of proteins identified as sacsin interactors were performed with stringApp for Cytoscape 3.8.

For the co-IP between NFL and sacsin, additional step was adopted from the protocol previously developed by Rao et al. to uncover the interaction between NFL and MyoVa (54). Briefly, SH-SY5Y cells were lysed in TritonX100 1%, TrisHCl pH 6.8 50 m, NaCl 200mM, glycerol 20%, EDTA 1mM with Douncer homogenizer; Triton-insoluble pellet was resuspended in Tris Buffered Saline and SDS 10% and NF cytoskeletal insoluble fraction was extracted by 1:4 dilution in NF extraction buffer (TrisHCl pH 7.4 60mM, NaCl 190mM, EDTA 6mM, Triton-X100 1.25%), prior to incubation with Dynabeads-antibody complexes.

Tissue lysis and antibodies for WB

For WBs, soluble fractions were obtained from tissues or cells by lysis in 100 mM Tris-HCl (pH 7.4), 1 mM EDTA (pH 8), 1% Triton X-100 and 150 mM NaCl supplemented with Protease Inhibitor Cocktail (PIC, Sigma-Aldrich, Merck KGaA) and Phosphatase Inhibitor Cocktail (Merck KGaA) using a Dounce homogenizer and incubated for 30' on ice. Cell debris were discarded by centrifugation at 8000 g for 10' at 4°C. To obtain insoluble fractions, tissues were homogenized in high ionic strength buffer (0,05 M MOPS pH 6.8, 1% Triton X-100 and 0,6 M KCl) and then centrifuged at 15000 g for 5' at RT. The triton insoluble pellet was treated with 0,5 µg/ml DNase I in 10 mM $MgCl_2$ buffer for 30' at 37°C. After washing, the pellet was solubilized in urea buffer (8 M urea in 0,1 M MOPS).

Commercially available antibodies were used for the detection of CaMKIIβ (sc-376828), pCaMKIIβ (sc-12886) and PCP2 (sc-137064; Santa Cruz Biotechnology Inc.), npNFH (SMI32, 801701; Biolegend), plectin (ab32528; Abcam), PSD95 (ab2723; Abcam), sacsin (ab181190; Abcam), IP3R1 (NB120-5908; Novus Biologicals), calbindin1 (214011; Synaptic System GmbH), GFAP (Z0334; Dako, Agilent), and calnexin (C4731; Sigma-Aldrich, Merck KGaA), myosin Va (LF-18, M4812; Sigma-Aldrich, Merck KGaA). Secondary antibodies included Horseradish Peroxidase (HRP)-conjugated anti-mouse and anti-rabbit IgG (Amersham Bioscience).

Ca^{2+} imaging

Ca^{2+} peaks were assayed with Calbryte 520 (AAT Bioquest). Cell loading was performed at 37°C (5 µM, 30') in HBSS 1X buffer. Images were acquired on a widefield Zeiss Axio-Observer.Z1 microscope equipped with a 20X objective lens (Carl Zeiss Microscopy). The evoked Ca^{2+}-response (fold change, $\Delta F/F_0$) was calculated as mean values within ROIs drawn in neuronal soma (Fiji software).

qRT-PCR

cDNA was generated using SuperScript IV Reverse Transcriptase kit (Invitrogen) and processed by qRT-PCR using the SYBR green chemistry (Light cycler 480, SYBR green I master, Roche).

To perform qRT-PCR were used the following primers (5'>3'):

Itpr1	FW - GGCTACAGGGCATTACTTGG	REV - GATGGAGGAGATGTCGTTGC
Calb1	FW - AGTTGGCTCACGTCTTACCC	REV - CTCTGTCAGTTCCAGCTTTCC
Casq2	FW - CACGTACGATGGGAAAGACC	REV - ATCCCAGCCTCTTAGCAAGC
Car8	FW - CTTGCAGCGAAGGAGTTACC	REV - GGTAGGTCGGAAATTGTCTC
Gfap	FW - GTGGAGAGGGACAACTTTGC	REV - CTCCTCCAGCGATTCAACC
Hprt1	FW - ACATTGTGGCCCTCTGTGTG	REV - TTATGTCCCCCGTTGACTGA

LFQ proteomics analysis

Mouse cerebellum (5 months of age) was lysed in 8 M Urea, 100 mM Tris-HCl pH 8 and PIC. Samples were processed by LFQ-MS/MS in collaboration with Cogentech proteomics facility (IFOM, Milan). To determine the significance of the differential proteins was used the cut-off determined by FDR < 0,05 (n=3 wild-type and 3 *Sacs*$^{-/-}$ mice, each in technical replicate). The significant deregulated proteins obtained in this way were submitted to GProfiler Enrichment analysis (https://biit.cs.ut.ee/gprofiler/gost).

Transcriptomics analysis

Standard RNA seq analysis was performed on total RNA extracted from cerebellum with RNeasy kit (Qiagen) (n=5 wild-type and 5 *Sacs*$^{-/-}$ mice). Libraries were prepared using True-Seq® stranded mRNA® for mRNA Sequencing (Illumina, San Diego, CA). Sequencing was performed on a NextSeq 500 machine (Illumina, San Diego, CA) obtaining 30 million single-end reads per sample on average. Only genes with a Counts per million (CPM) value higher than 1 in at least three samples were retained. Gene expression read counts were exported and analysed in R environment (v. 3.6.2) to identify differentially expressed genes (DEGs). The DEG analysis was performed with the package DESeq2 available in Bioconductor comparing different experimental groups. To determine the significance of the differential genes was used the cut-off determined by FDR filter < 0,1 (Adjusted p_value). The significant deregulated genes obtained with this algorithm were submitted to GProfiler Enrichment analysis.

Animals and Ceftriaxone treatments

Sacs$^{-/-}$ and wild-type littermates were obtained by breeding *Sacs*$^{+/-}$ male and female mice (C57BL/6). Ceftriaxone (Fidia Farmaceutici) was administered monthly by daily i.p injection at the dose of 200 mg/kg body weight for 5 consecutive days as previously described.(18) The pre-clinical trials were performed in accordance with experimental protocols approved by the IACUC of San Raffaele Scientific Institute.

Behavioural tests

BW test to assess motor balance was performed for 3 consecutive days (in each day the mice performed 3 trials on the beam, 7mm x 90cm suspended 40cm above bedding), after two days of training. The number of hindfoot missteps and the time required to cross the beam (latency) was evaluated, as previously described (55). The mean of all the trials was scored. Animal behavioural testing was performed by investigators blinded to the group of the mice, the

analysis was performed by two independent investigators analysing videorecording of the motor tests.

Histological analyses

Tissues were fixed after perfusion in 4% paraformaldehyde-2,5M glutaraldehyde in 0,12M cacodylate buffer solution. 1µm semithin sections of cerebellum were cut and stained with toluidine blue. Images of anterior lobules of cerebellum were acquired on Olympus BX51 microscope equipped with a 20X objective lens (Leica Microsystems).

Statistics

For statistical evaluation of phenotypes (imaging, WB) in *Sacs*$^{-/-}$ cells or mice compared with wild-type controls, we performed Unpaired Student's t-test, 2-tails (applying Welch's correction). For behavioural tests, power analysis for sample size estimation was performed using G*Power (v. 3.1) software based on previous data to achieve power set at 80% and significance level at 0,05. Regarding pharmacological treatment with Ceftriaxone, for statistical comparisons we applied Two-way ANOVA and Tukey's multicomparison test (GraphPad Prism software, https://www.graphpad.com/scientific-software/prism/).

Study approval

The pre-clinical trials with Ceftriaxone were approved by and performed in accordance with experimental protocols approved by the IACUC of San Raffaele Scientific Institute.

Data availability

Raw RNA seq data have been uploaded in GEO repository (GSE200876), and proteomics data have been uploaded in PRIDE repository (PXD033385).

Author contribution

FM, ADB and FL conceptualized the study. FM, ADB, FL designed the study methodology. ADB, FL, DDR, ES, PP, AB performed experiments. FM, ADB, FL, DDR, ES, AQ analyzed

data. FM acquired funds. AB, AQ and BB provided expertise and feedback. FM and ADB wrote the manuscript. All authors reviewed the manuscript.

Acknowledgements

We acknowledge the San Raffaele facilities ALEMBIC and in particular Valeria Berno for images acquisition and analysis, the Center of OMICS Science and the IFOM facility Cogentech. We are grateful to Helene Puccio and Stefano Previtali for critical discussion. We thank Marco Bacigaluppi and Giorgia Gullotta for advice and comments on astrocyte and microglia data. The project was funded by: Italian Ministry of Health, RF-2016-02361610 and RF-2019-12370417 (FM); Italian Ministry of Health European Joint Programme on Rare Diseases 2021, grant Treat-ARCA (FM); Ataxia Charlévoix-Saguenay Foundation (FM); Fondazione Centro San Raffaele- Fronzaroli fellowship program (ADB & FL).

References

1. Bouchard JP. Recessive spastic ataxia of Charlevoix-Saguenay. Elsevier Science, Amsterdam. 1991;16(Hereditary neuropathies and spinocerebellar atrophies. Handbook of clinical neurology):451–9.
2. Synofzik M, Nemeth AH. Recessive ataxias. Handb Clin Neurol. 2018;155:73-89.
3. Xiromerisiou G, et al. A novel homozygous SACS mutation identified by whole exome sequencing-genotype phenotype correlations of all published cases. J Mol Neurosci. 2020;70(1):131-41.
4. Engert JC, et al. ARSACS, a spastic ataxia common in northeastern Quebec, is caused by mutations in a new gene encoding an 11.5-kb ORF. Nat Genet. 2000;24(2):120-5.
5. Parfitt DA, et al. The ataxia protein sacsin is a functional co-chaperone that protects against polyglutamine-expanded ataxin-1. Hum Mol Genet. 2009;18(9):1556-65.
6. Lariviere R, et al. Sacs R272C missense homozygous mice develop an ataxia phenotype. Mol Brain. 2019;12(1):19.
7. Girard M, et al. Mitochondrial dysfunction and Purkinje cell loss in autosomal recessive spastic ataxia of Charlevoix-Saguenay (ARSACS). Proc Natl Acad Sci U S A. 2012;109(5):1661-6.
8. Lariviere R, et al. Sacs knockout mice present pathophysiological defects underlying autosomal recessive spastic ataxia of Charlevoix-Saguenay. Hum Mol Genet. 2015;24(3):727-39.
9. Anderson JF, Siller E, Barral JM. The sacsin repeating region (SRR): a novel Hsp90-related supra-domain associated with neurodegeneration. J Mol Biol. 2010;400(4):665-74.

10. Greer PL, et al. The Angelman Syndrome protein Ube3A regulates synapse development by ubiquitinating arc. Cell. 2010;140(5):704-16.
11. Kozlov G, et al. Structural basis of defects in the sacsin HEPN domain responsible for autosomal recessive spastic ataxia of Charlevoix-Saguenay (ARSACS). J Biol Chem. 2011;286(23):20407-12.
12. Duncan EJ, et al. Altered organization of the intermediate filament cytoskeleton and relocalization of proteostasis modulators in cells lacking the ataxia protein sacsin. Hum Mol Genet. 2017;26(16):3130-43.
13. Bradshaw TY, et al. A reduction in Drp1-mediated fission compromises mitochondrial health in autosomal recessive spastic ataxia of Charlevoix Saguenay. Hum Mol Genet. 2016.
14. Criscuolo C, et al. Powerhouse failure and oxidative damage in autosomal recessive spastic ataxia of Charlevoix-Saguenay. J Neurol. 2015;262(12):2755-63.
15. Gentil BJ, et al. Sacsin, mutated in the ataxia ARSACS, regulates intermediate filament assembly and dynamics. FASEB J. 2019;33(2):2982-94.
16. Kano MW, M. Cerebellar circuits. Neural Circuit and Cognitive Development (Second Edition). 2020:79-102.
17. Rothstein JD, et al. Beta-lactam antibiotics offer neuroprotection by increasing glutamate transporter expression. Nature. 2005;433(7021):73-7.
18. Maltecca F, et al. Purkinje neuron Ca2+ influx reduction rescues ataxia in SCA28 model. J Clin Invest. 2015;125(1):263-74.
19. Longo F, et al. Assessment of Sacsin Turnover in Patients With ARSACS: Implications for Molecular Diagnosis and Pathogenesis. Neurology. 2021;97(23):e2315-e27.
20. Sheng ZH, Cai Q. Mitochondrial transport in neurons: impact on synaptic homeostasis and neurodegeneration. Nat Rev Neurosci. 2012;13(2):77-93.
21. Schwarz TL. Mitochondrial trafficking in neurons. Cold Spring Harb Perspect Biol. 2013;5(6).
22. Popov LD. Mitochondrial biogenesis: An update. J Cell Mol Med. 2020;24(9):4892-9.
23. Miyata M, et al. Local calcium release in dendritic spines required for long-term synaptic depression. Neuron. 2000;28(1):233-44.
24. Wagner W, Brenowitz SD, Hammer JA, 3rd. Myosin-Va transports the endoplasmic reticulum into the dendritic spines of Purkinje neurons. Nat Cell Biol. 2011;13(1):40-8.
25. Winter L, Wiche G. The many faces of plectin and plectinopathies: pathology and mechanisms. Acta Neuropathol. 2013;125(1):77-93.
26. Valencia RG, et al. Plectin dysfunction in neurons leads to tau accumulation on microtubules affecting neuritogenesis, organelle trafficking, pain sensitivity and memory. Neuropathol Appl Neurobiol. 2021;47(1):73-95.
27. Weiss A, et al. Sensitive biochemical aggregate detection reveals aggregation onset before symptom development in cellular and murine models of Huntington's disease. J Neurochem. 2008;104(3):846-58.
28. Hartmann J, Konnerth A. Determinants of postsynaptic Ca2+ signaling in Purkinje neurons. Cell Calcium. 2005;37(5):459-66.
29. Datta S, Jaiswal M. Mitochondrial calcium at the synapse. Mitochondrion. 2021;59:135-53.
30. Hudmon A, Schulman H. Neuronal CA2+/calmodulin-dependent protein kinase II: the role of structure and autoregulation in cellular function. Annu Rev Biochem. 2002;71:473-510.
31. Araujo APB, Carpi-Santos R, Gomes FCA. The Role of Astrocytes in the Development of the Cerebellum. Cerebellum. 2019;18(6):1017-35.
32. Yimer EM, Hishe HZ, Tuem KB. Repurposing of the beta-Lactam Antibiotic, Ceftriaxone for Neurological Disorders: A Review. Front Neurosci. 2019;13:236.

33. Tai CH, et al. A new avenue for treating neuronal diseases: Ceftriaxone, an old antibiotic demonstrating behavioral neuronal effects. Behav Brain Res. 2019;364:149-56.
34. Sicot G, et al. Downregulation of the Glial GLT1 Glutamate Transporter and Purkinje Cell Dysfunction in a Mouse Model of Myotonic Dystrophy. Cell Rep. 2017;19(13):2718-29.
35. Schwarz N, Leube RE. Intermediate Filaments as Organizers of Cellular Space: How They Affect Mitochondrial Structure and Function. Cells. 2016;5(3).
36. Gentil BJ, Tibshirani M, Durham HD. Neurofilament dynamics and involvement in neurological disorders. Cell Tissue Res. 2015;360(3):609-20.
37. Israeli E, et al. Intermediate filament aggregates cause mitochondrial dysmotility and increase energy demands in giant axonal neuropathy. Hum Mol Genet. 2016;25(11):2143-57.
38. Wagner OI, et al. Mechanisms of mitochondria-neurofilament interactions. J Neurosci. 2003;23(27):9046-58.
39. Francis V, et al. The ARSACS disease protein sacsin controls lysosomal positioning and reformation by regulating microtubule dynamics. J Biol Chem. 2022;298(9):102320.
40. Winter L, Abrahamsberg C, Wiche G. Plectin isoform 1b mediates mitochondrion-intermediate filament network linkage and controls organelle shape. J Cell Biol. 2008;181(6):903-11.
41. Hammer JA, 3rd, Wagner W. Functions of class V myosins in neurons. J Biol Chem. 2013;288(40):28428-34.
42. Egorova P, Popugaeva E, Bezprozvanny I. Disturbed calcium signaling in spinocerebellar ataxias and Alzheimer's disease. Semin Cell Dev Biol. 2015;40:127-33.
43. Prestori F, Moccia F, D'Angelo E. Disrupted Calcium Signaling in Animal Models of Human Spinocerebellar Ataxia (SCA). Int J Mol Sci. 2019;21(1).
44. Shimobayashi E, Kapfhammer JP. Calcium Signaling, PKC Gamma, IP3R1 and CAR8 Link Spinocerebellar Ataxias and Purkinje Cell Dendritic Development. Curr Neuropharmacol. 2018;16(2):151-9.
45. Hickman S, et al. Microglia in neurodegeneration. Nat Neurosci. 2018;21(10):1359-69.
46. Kwon HS, Koh SH. Neuroinflammation in neurodegenerative disorders: the roles of microglia and astrocytes. Transl Neurodegener. 2020;9(1):42.
47. Ferro A, et al. Role of Microglia in Ataxias. J Mol Biol. 2019;431(9):1792-804.
48. Lee SG, et al. Mechanism of ceftriaxone induction of excitatory amino acid transporter-2 expression and glutamate uptake in primary human astrocytes. J Biol Chem. 2008;283(19):13116-23.
49. Bachetti T, et al. In vitro treatments with ceftriaxone promote elimination of mutant glial fibrillary acidic protein and transcription down-regulation. Exp Cell Res. 2010;316(13):2152-65.
50. Ho YJ, et al. Ceftriaxone Treatment for Neuronal Deficits: A Histological and MEMRI Study in a Rat Model of Dementia with Lewy Bodies. Behav Neurol. 2018;2018:4618716.
51. Cudkowicz ME, et al. Safety and efficacy of ceftriaxone for amyotrophic lateral sclerosis: a multi-stage, randomised, double-blind, placebo-controlled trial. Lancet Neurol. 2014;13(11):1083-91.
52. Mijalkovic J, et al. Ensemble and single-molecule dynamics of IFT dynein in Caenorhabditis elegans cilia. Nat Commun. 2017;8:14591.
53. Maltecca F, et al. The mitochondrial protease AFG3L2 is essential for axonal development. J Neurosci. 2008;28(11):2827-36.
54. Rao MV, et al. Myosin Va binding to neurofilaments is essential for correct myosin Va distribution and transport and neurofilament density. J Cell Biol. 2002;159(2):279-90.
55. Maltecca F, Magnoni R, Cerri F, Cox GA, Quattrini A, Casari G. Haploinsufficiency of AFG3L2, the gene responsible for spinocerebellar ataxia type 28, causes mitochondria-mediated Purkinje cell dark degeneration. J Neurosci. 2009;29(29):9244-54.

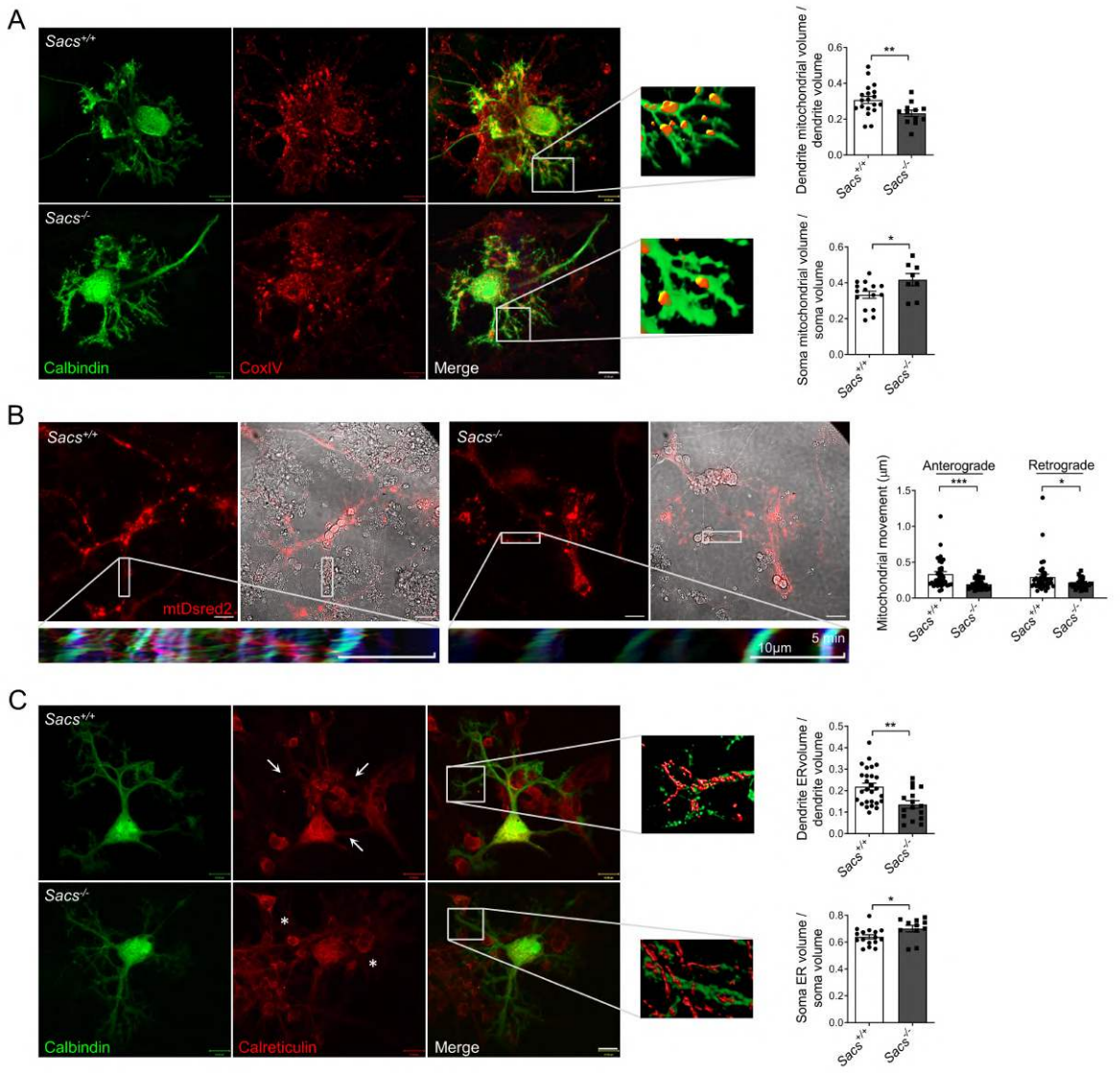

Figure 1. Defective mitochondrial and ER distribution in distal processes of *Sacs*$^{-/-}$ primary PCs. (**A**) Representative confocal images (63X) and higher magnification rendering of distal dendrites *Sacs*$^{-/-}$ and wild-type PCs at DIV15 stained in green with calbindin and in red with the mitochondrial marker CoxIV. Scale bar=13µm. Graphs represent volumetric quantification of dendritic or soma mitochondrial volume (normalized to dendrite/soma volume). Bars represent mean±SEM; n=at least 9 from at least 5 independent experiments; Welch's t-test: **P*<0,05, ***P*<0,01; (**B**) Representative images (60X) of *Sacs*$^{-/-}$ and wild-type PC dendrites at DIV10 after infection with mtDsred2 lentivirus. Scale bar=20µm. Kymographs were derived by 30 minutes of live imaging (1 frame/minute) using KymographClear (ImageJ). The kymographs are relative to the dendrite highlighted into the white boxes (the orientation is with soma to the left). Colour code: in red the anterograde movement, in green retrograde movement and in blue the still mitochondria. Graphs represent the average anterograde or retrograde displacement per minute along dendrite longitudinal axis of each mitochondrion. Bars represent mean±SEM; n=at least 34 from at least 3 independent experiments; Welch's t-test: **P*<0,05, ****P*<0,001; (**C**) Representative confocal images (63X) and higher magnification rendering of distal dendrites *Sacs*$^{-/-}$ and wild-type PCs at DIV15 stained in green with calbindin and in red with the ER marker calreticulin. Scale bar=13µm. Graphs represent volumetric quantification of dendritic or soma ER volume (normalized to dendrite/soma volume). Bars represent mean±SEM; n=at least 11 from at least 6 independent experiments; Welch's t-test: **P*<0,05, ***P*<0,01.

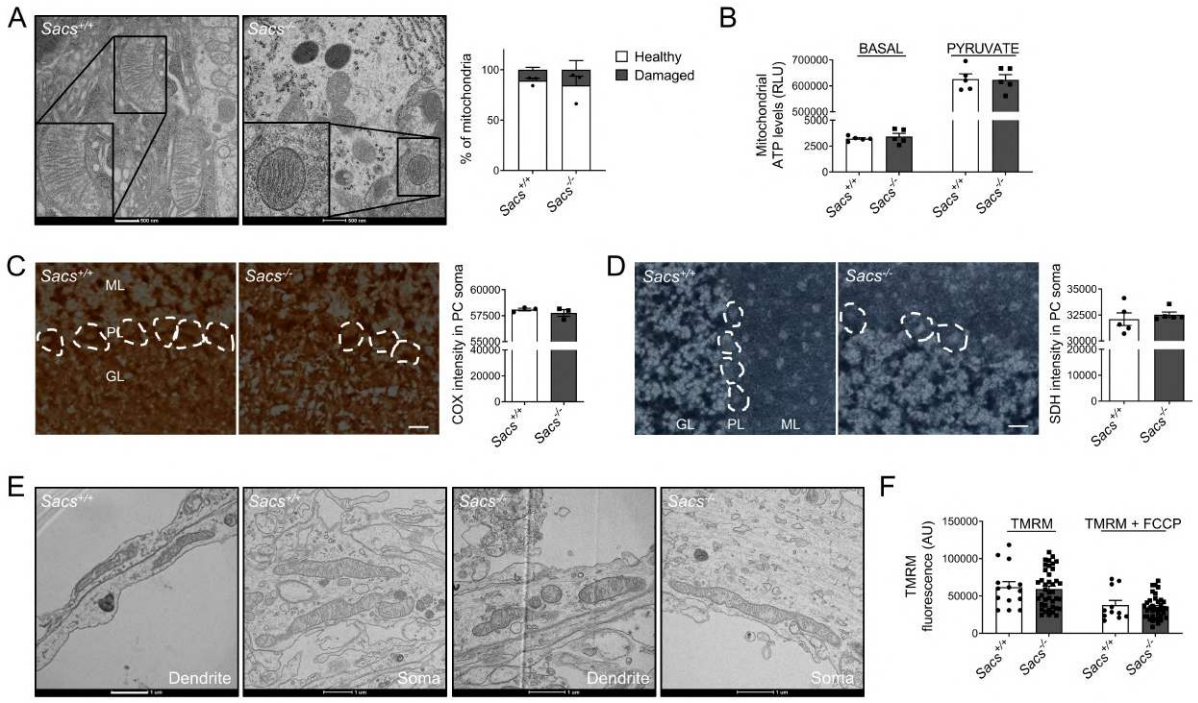

Figure 2. In vivo and ex vivo *Sacs*$^{-/-}$ PCs show unaltered mitochondrial ultrastructure and normal mitochondrial metabolism. (**A**) Representative EM images (150.000X magnification) and relative quantitation of PC showing intact inner- and outer mitochondrial membrane in *Sacs*$^{-/-}$ PCs at 5 months of age. Scale bar=500nm. Bars represent mean±SEM; n=3; Welch's t-test: ns; (**B**) ATP production analysis in freshly isolated mitochondria from mouse cerebellum at 5 months of age at basal level and upon pyruvate stimulation. Bars represent mean±SEM; n=5; Welch's t-test: ns; (**C-D**) Colorimetric activity assay for COX (C) and SDH (D) in fresh cerebellar slices in PC soma of *Sacs*$^{-/-}$ and wild-type mice at 5 months of age (ML:Molecular layer, PL:Purkinje cell layer, GL:Granule cell layer). Scale bar=25µm. Graph represents intensity staining values as mean±SEM; n=3 (at least 4 images per sample and at least 4 cells per image); Welch's t-test: ns; (**E**) Representative EM images (150.000X magnification) of primary PC showing intact mitochondrial ultrastructure in *Sacs*$^{-/-}$ PCs at DIV15 (both in soma and processes). Scale bar=1µm; (**F**) Analysis of $\Delta\Psi_{mito}$ by live-imaging measurement of TMRM fluorescence intensity in DIV15 primary PC soma. Bars represent mean±SEM; n=at least 14 from at least 4 independent experiments; Welch's t-test: ns.

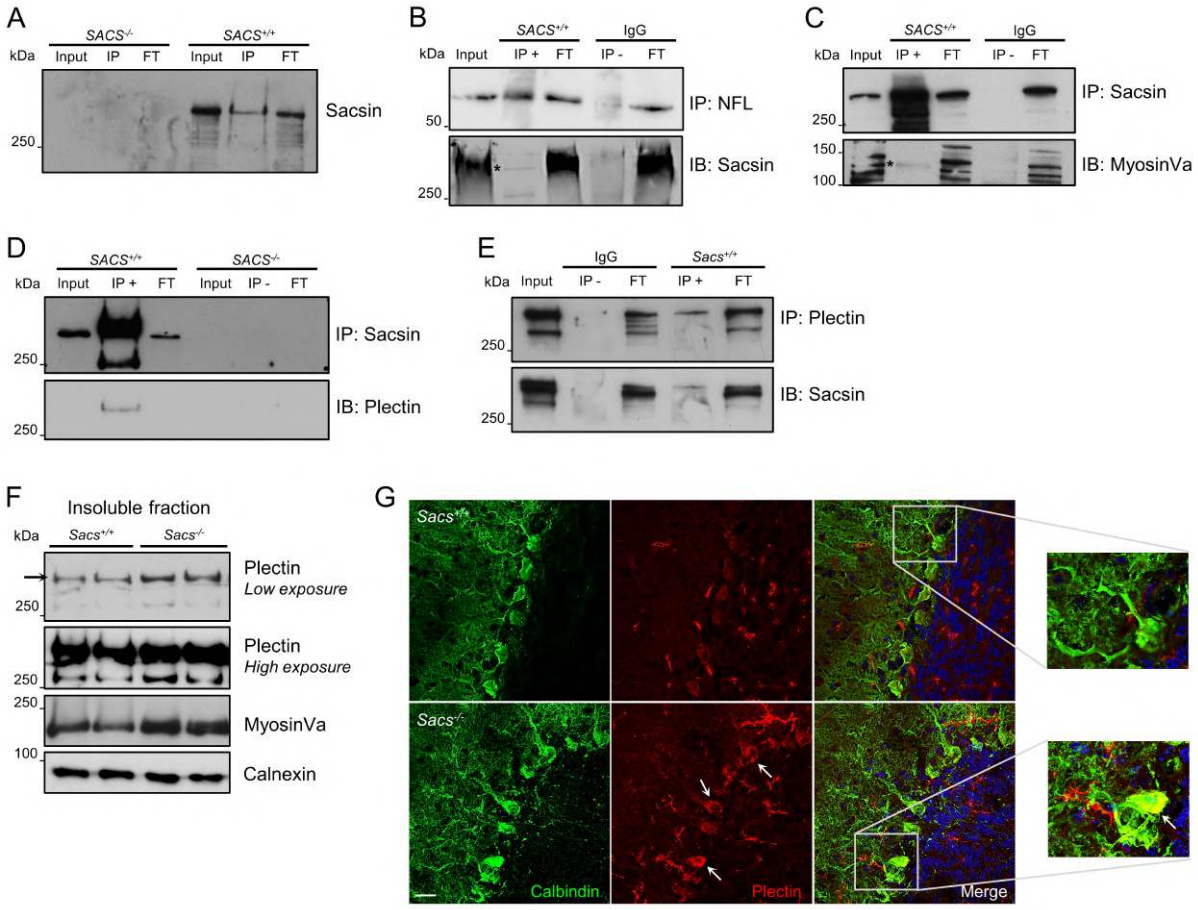

Figure 3. Sacsin physically interacts with plectin and myosin Va, whose levels are deregulated in sacsin-depleted cells and cerebellum. (**A**) Sacsin immunoprecipitation in SH-SY5Y cells (IP=Immunoprecipitation, FT=Flow Through); (**B**) NFL IP in SH-SY5Y cells (with IgG as control) and immunodecoration with anti-sacsin antibody (asterisk indicates the specific band); (**C-D**) Sacsin IP in SH-SY5Y cells (with IgG and *SACS*$^{-/-}$, respectively, as control) and immunodecoration with anti-myosin Va (asterisk indicates the specific band; C) and anti-plectin (D) antibodies; (**E**) Plectin IP in wild-type cerebellum (with IgG as control) and immunodecoration with anti-sacsin antibody; (**F**) WB analysis showing levels of plectin and myosin Va in insoluble fractions of *Sacs*$^{-/-}$ and wild-type cerebellum (normalized to calnexin); (**G**) Representative images (60X) of cerebellar slices stained with calbindin (in green) and plectin (in red) showing a more intense plectin signal in *Sacs*$^{-/-}$ PC soma and proximal dendrites compared to wild-type controls. Scale bar=20µm.

Table in Figure 3: LFQ intensities of selected sacsin cytoskeletal interactors.

Protein names	Gene names	LFQ intensity WT_01	LFQ intensity WT_01R	LFQ intensity KO_01	LFQ intensity KO_01R
Neurofilament medium polypeptide	NEFM	29,61626	29,46205	NaN	NaN
Neurofilament light polypeptide	NEFL	28,42306	28,3917	NaN	NaN
Plectin	PLEC	28,22972	28,00646	NaN	NaN
Unconventional myosin-Va	MYO5A	28,63903	28,66119	NaN	NaN

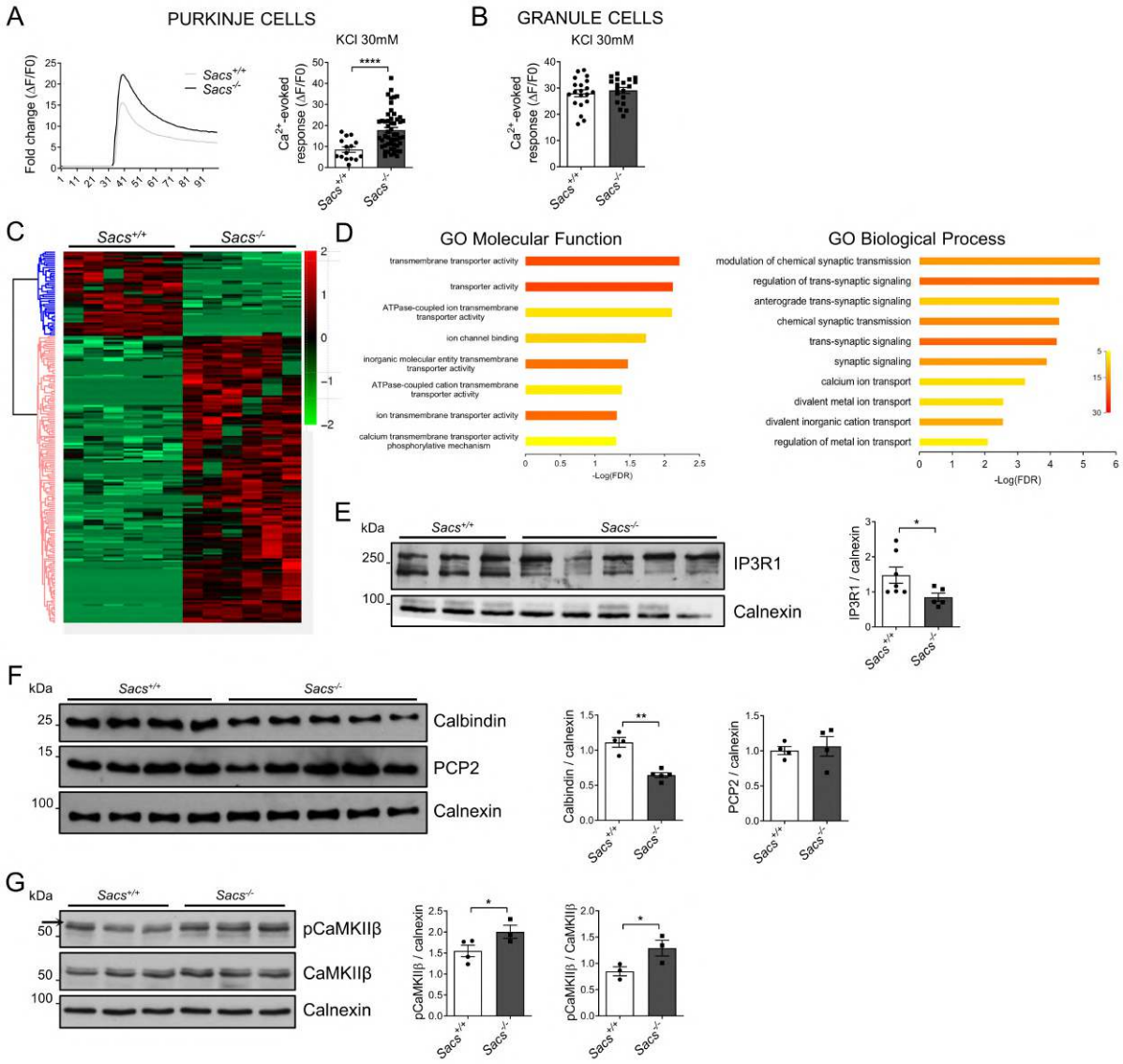

Figure 4. Ca^{2+} deregulation in *Sacs*$^{-/-}$ primary PCs and cerebellum. (**A**) Representative traces of cytosolic Ca^{2+} responses before and after KCl stimulation of *Sacs*$^{-/-}$ and wild-type control primary PCs. Graph shows PC Ca^{2+}-evoked responses after stimulation with 30 mM KCl (normalized increase measured above the initial value). Bars represent mean±SEM; n= at least 15 from at least 5 independent experiments; Welch's t-test: ****P<0,0001; (**B**) Granule cell Ca^{2+}-evoked responses after stimulation with 30 mM KCl (normalized increase measured above the initial value). Bars represent mean±SEM; n=at least 19 from at least 5 independent experiments; Welch's t-test: ns; (**C**) Heatmap of cerebellar protein profile comparing *Sacs*$^{-/-}$ and wild-type controls at 5 months of age; n=6 from 3 biological replicates; (**D**) GProfiler enrichment of deregulated proteins comparing 5 months-old *Sacs*$^{-/-}$ and wild-type cerebellum, showing the top 10 categories for each GO: molecular function (MF) and biological process (BP); (**E-G**) WB analysis showing levels of IP3R1 (E), Calbindin and PCP2 (F) and pCaMKIIβ (upper band as indicated by the arrow) and CaMKIIβ (G) in *Sacs*$^{-/-}$ and wild-type control cerebellum at 5 months of age with relative quantitation (normalized to calnexin). Bars represent mean±SEM; n=at least 4; Welch's t-test: *P <0,05, **P <0,01.

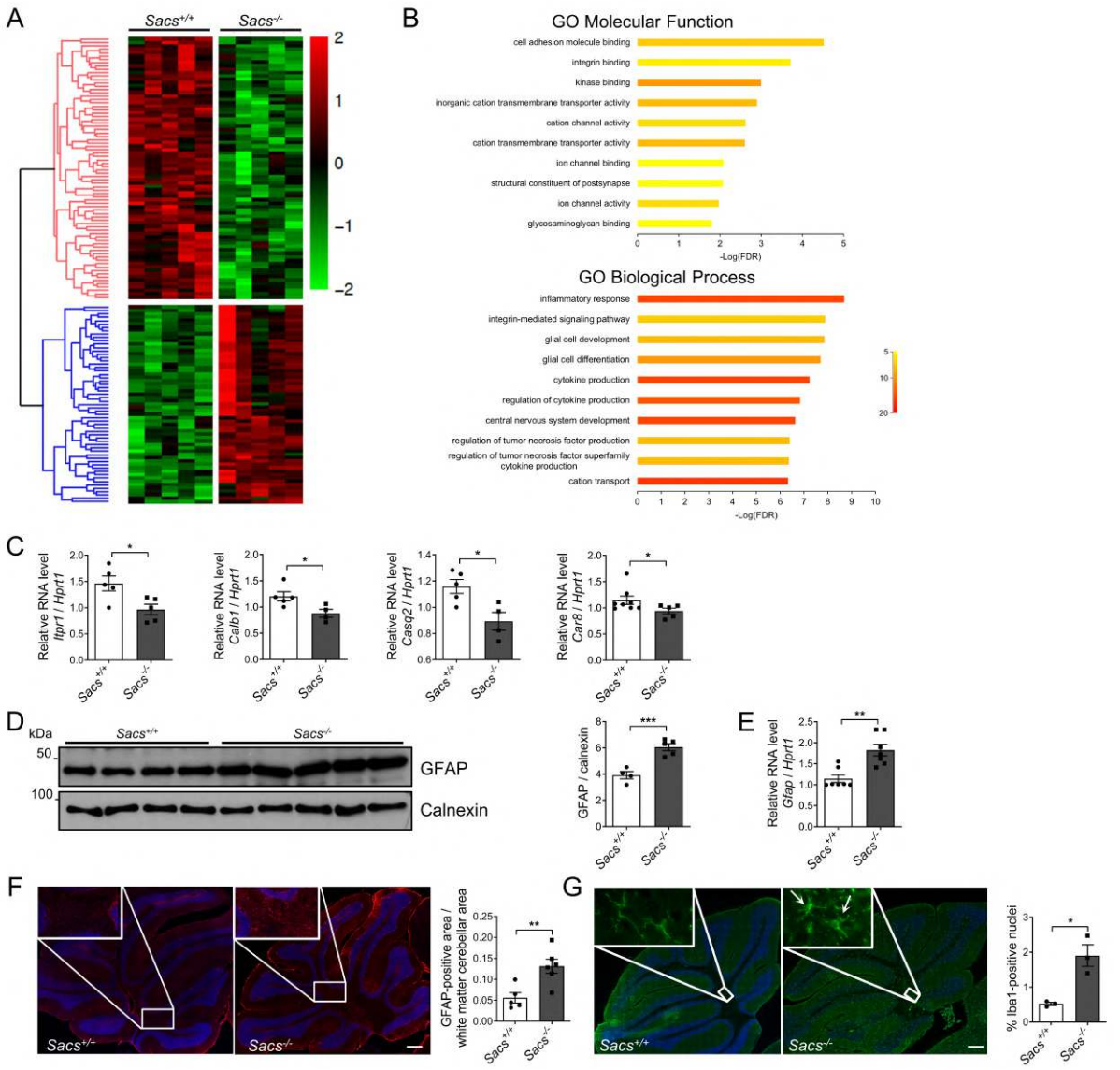

Figure 5. Transcriptomics analysis supports Ca^{2+} deregulation and neuroinflammation in *Sacs*$^{-/-}$ cerebellum. (**A**) Heatmap of cerebellar gene expression profile comparing *Sacs*$^{-/-}$ and wild-type mice at 5 months of age; n=5; (**B**) GProfiler enrichment of deregulated genes comparing 5 months-old *Sacs*$^{-/-}$ and wild-type cerebellum showing the top 10 categories for each GO: molecular function (MF) and biological process (BP); (**C**) qRT-PCR showing levels of *Itpr1*, *Calb1*, *Casq2* and *Car8* mRNA (relative to *Hprt1* mRNA) in *Sacs*$^{-/-}$ and wild-type cerebellum at 5 months of age. Bars represent mean±SEM; n=5; Welch's t-test: * P <0,05; (**D**) WB analysis showing levels of GFAP in *Sacs*$^{-/-}$ and wild-type control cerebellum at 5 months of age with relative quantitation (normalized to calnexin). Bars represent mean±SEM; n=at least 4; Welch's t-test: ***P <0,001; (**E**) qRT-PCR showing levels of *Gfap* mRNA (relative to *Hprt1* mRNA) in *Sacs*$^{-/-}$ and control cerebellum at 5 months of age. Bars represent mean±SEM; n=5; Welch's t-test: **P<0,01; (**F**) Representative images of immunofluorescence analysis showing astrocyte activation (GFAP, in red) in 5 months-old *Sacs*$^{-/-}$ cerebellum compared to controls. Scale bar=0,2mm. Bars represent mean±SEM; n=3; Welch's t-test: **P<0,01; (**G**) Representative images of immunofluorescence staining of microglia by Iba1 (in green) highlighting microglial morphological shift in 5 months-old *Sacs*$^{-/-}$ cerebellum compared with wild-type controls. Arrows indicate the amoeboid-phagocytic phenotype of microglia. Quantitative analysis of the percentage of Iba1-positive cells was normalized to the total nuclei number. Scale bar=0,2mm. Bars represent mean±SEM; n=3; Welch's t-test: *P <0,05.

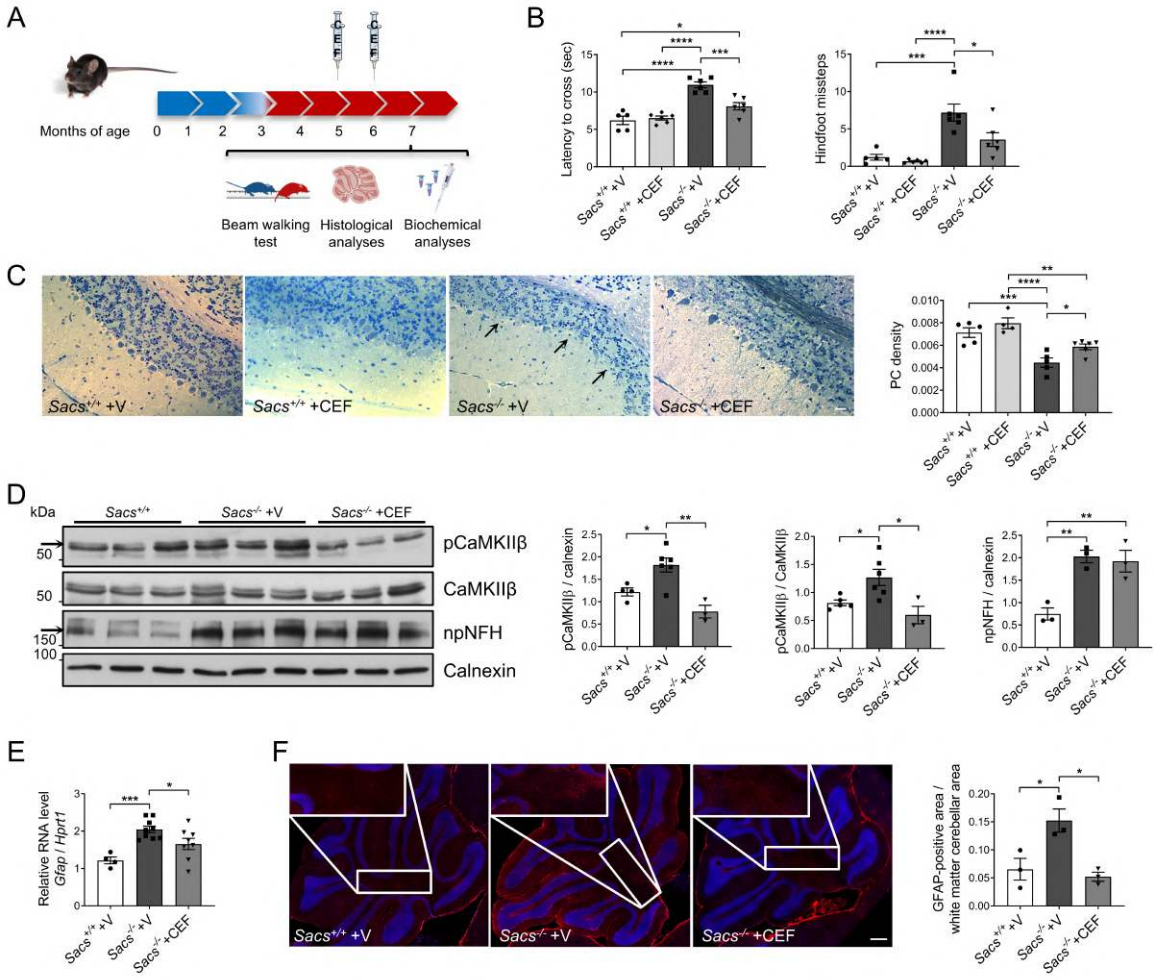

Figure 6. Post- symptomatic Ceftriaxone treatment improves motor coordination, delays PC loss and mitigates Ca^{2+} deregulation in *Sacs*$^{-/-}$ cerebellum. (**A**) Schematic representation of pre-clinical post-symptomatic Ceftriaxone administration protocol; (**B**) BW test performance in term of latency time to cross the beam and number of hindfoot missteps of female mice of the indicated genotypes, Ceftriaxone- and vehicle-treated, at 7 months of age. Bars represent mean±SEM; n= at least 5; Two-way ANOVA with Tukey's correction: **P* <0,05, ****P* <0,001, *****P* <0,0001; (**C**) Representative semithin sections of cerebellum of Ceftriaxone- and vehicle-treated mice of the indicated genotype, with relative quantitation of PC density at 7 months. Scale bar=25µm. Bars represent mean±SEM; n=at least 4 (10 images per sample); Two-way ANOVA with Tukey's correction: **P*<0,05, ***P*<0,01, ****P*<0,001, *****P*<0,0001; (**D**) WB analysis showing levels of pCaMKIIβ (upper band as indicated by the arrow), CaMKIIβ and npNFH in wild-type, vehicle- and Ceftriaxone-treated *Sacs*$^{-/-}$ cerebellum at 7 months of age with relative quantitation (normalized to calnexin). Bars represent mean±SEM; n=at least 3; Two-way ANOVA with Tukey's correction: **P* <0,05, ***P* <0,01; (**E**) qRT-PCR showing levels of *Gfap* mRNA (relative to *Hprt1* mRNA) in wild-type, vehicle- and Ceftriaxone-treated *Sacs*$^{-/-}$ cerebellum at 7 months of age. Bars represent mean±SEM; n=at least 4; Two-way ANOVA with Tukey's correction: **P*<0,05, ****P* <0,001; (**F**) Representative images of immunofluorescence analysis showing astrocytes (GFAP, in red) in 7 months of age Ceftriaxone- and vehicle-treated *Sacs*$^{-/-}$ and wild-type control cerebellum. Bars represent mean±SEM; n=3; Two-way ANOVA with Tukey's correction: **P*<0,05.

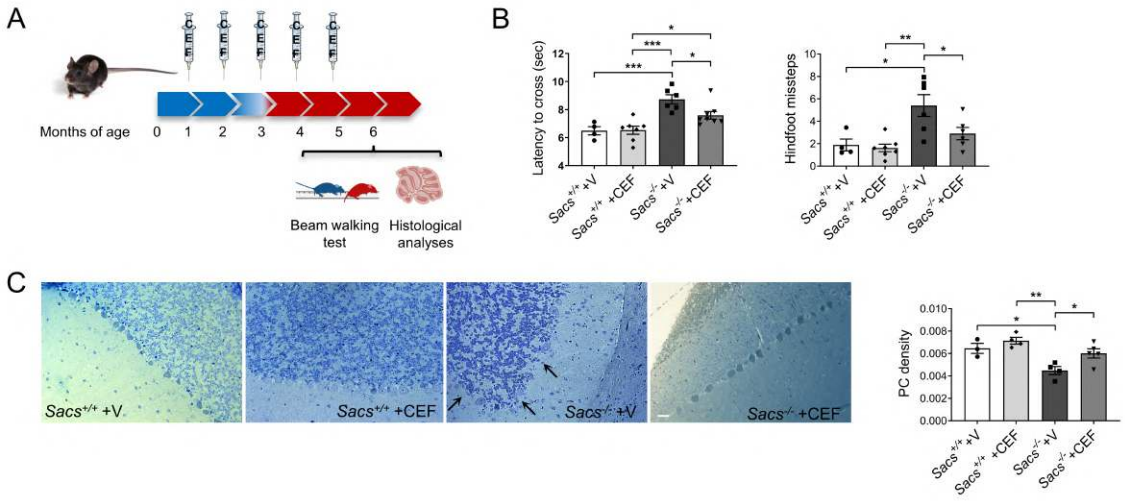

Figure 7. Pre-symptomatic Ceftriaxone treatment improves motor coordination, delays PC loss in *Sacs*$^{-/-}$ mice. (**A**) Schematic representation of pre-clinical pre-symptomatic Ceftriaxone administration protocol; (**B**) BW test performance in term of latency time to cross the beam and number of hindfoot missteps at 6 months of age female Ceftriaxone- and vehicle-treated mice. Bars represent mean±SEM; n= at least 5; Two-way ANOVA with Tukey's correction: **P*<0,05, ***P*<0,01, ****P*<0,001; (**C**) Representative semithin section of 6 months-old cerebellum of Ceftriaxone- and vehicle-treated mice with relative quantitation of PC density. Scale bar=25µm. Bars represent mean±SEM; n=at least 4 (10 images per sample); Two-way ANOVA with Tukey's correction: **P*<0,05, ***P*<0,01.